

Optimisation of camera positions for optical coordinate measurement based on visible point analysis

Hui Zhang^{1,2}, Joe Eastwood², Mohammed Isa², Danny Sims-Waterhouse³, Richard Leach^{2,3} and Samanta Piano²

¹School of Mechanical Engineering, Jiangsu University of Science and Technology, China

²Manufacturing Metrology Team, Faculty of Engineering, University of Nottingham, UK

³Taraz Metrology, UK

Abstract

In optical coordinate measurement using cameras, the number of images, and positions and orientations of the cameras, are critical to object accessibility and the accuracy of a measurement. In this paper, we propose a technique to optimise the number of cameras and the positions of these cameras for the measurement of a given object using visible point analysis of the object's computer aided design data. The visible point analysis technique is based on a hidden point removal approach; this technique is used to detect which surface points on the object are visible from a given camera position. A genetic algorithm is used to find the set of positions that provide optimum surface point density and overlap between views, while minimising the total number of camera images required. The genetic algorithm is used to minimise the measurement data processing time while maintaining optimum surface point density. We test this optimisation procedure on four artefacts and the measurements are shown to be comparable to that from a traceable contact co-ordinate measurement machine. We show that using our procedure improves the measurement quality compared to the more conventional approach of using equally spaced images. This work is part of a larger effort to fully automate and optimise optical coordinate measurement techniques.

Key words: optical coordinate measurement, camera pose optimisation, visible point analysis

1. Introduction

Optical coordinate measurement is becoming popular in manufacturing due to its non-contact nature, high point density, fast data acquisition rates, and relatively high measurement accuracy. With the decreasing prices of optical hardware, such as cameras and projectors, and a large number of complex measurement demands, optical coordinate measurement is used in a number of sectors, including aerospace [1], civil engineering [2], experimental solid mechanics [3] and additive manufacturing [4]

A typical optical coordinate measurement procedure involves firmware setup, camera positioning, image acquisition, image processing, reconstruction and data analysis [5]. Although optical coordinate

measurement has taken a market share in industrial inspection, the approach lacks an established and automated method for inspection planning; something that is common for contact coordinate measuring machines (CMMs) [6, 7]. Camera positioning is one of the most significant issues that makes the use of optical coordinate measurement systems (CMSs) restricted to experienced operators [8]. Optimal camera positioning is critical because the selected positions affect not only the image acquisition time and post processing of the data, but also the coverage of the object surfaces and the accuracy of the measurement. Published solutions to camera positioning in optical CMSs [8-12] are often application specific and the number of cameras is given in advance.

In this paper, a novel technique is proposed for determining optimal camera positions based on a visible point analysis approach. A genetic algorithm (GA) is adopted to find the optimal combination of camera positions that results in high surface coverage of an object while minimising the total number of cameras required. GAs are inspired by the mechanism of natural selection, where the best candidates from a population of possible solutions are chosen for further crossover and mutation to obtain new successors [13-15]. The process of generating new populations from descendants is repeated until the new population of successors converge. Since their introduction, GAs and their variants have been used in many areas and shown to be effective for non-linear, complex global optimisation problems (for examples, see the reviews [16, 17]). GAs are especially useful in poorly understood scenarios where there is no direct relationship between the input arguments and output target values, and for problems with large search spaces. Due to the complex search space when dealing with multiple cameras, GAs are promising candidates for camera position optimisation [18].

1.1 Related work

Optical coordinate measurement using cameras is now widely used in advanced manufacturing [19]. The use of a single stereo-pair of cameras, is often insufficient for part inspection due to the limited field of view (FOV) and the self-occlusion of surfaces [20]. In order to increase the FOV and maximise coverage of an object's surface, a network of multiple camera viewpoints can be an effective solution [24], which can be achieved using either multiple cameras or a single camera which moves relative to the object. The approach of using multiple views extends beyond large scale form metrology and has also been applied to microscopic scales [25]. Characterisation of the intrinsic and extrinsic camera parameters is critical for accurate measurement [19]. Camera calibration is a research topic in its own right and is beyond the scope of this work (for more details see [19-23]). Barazzetti points out [10] that as optical coordinate measurement, particularly photogrammetry, has become more accessible, inexperienced users with little measurement experience often produce crude reconstructions at the cost of metric accuracy. Particularly, inexperienced users are liable to capture far more images than are required with an unfavourable network geometry – this highlights the need for automated view planning.

There are two main concerns when view planning for an optical measurement system: where should the camera views be placed relative to the object, and how many camera views are required to satisfy object coverage and reconstruction accuracy requirements in reasonable amount of time [26]? Carrivick et al. [26] found that tens to hundreds of images are typically required for accurate reconstruction, depending on object complexity, desired reconstruction accuracy, and reconstruction time constraints. In a multi-camera network, as the number of cameras increases, so does the computational cost and bandwidth required; therefore, many state-of-the-art systems attempt to minimise the number of cameras in the network [23].

Early work in this field explored the development of the 'configuration of sensors' (CONSENS) system [7]; this used expert knowledge to conduct view planning from the CAD data of an object. The

'evolving position of cameras' (EPOCA) system [27] was developed for designing imaging networks for robotic systems. EPOCA did not rely on expert knowledge and instead used GAs to optimise the imaging network. More recently, the imaging network designer (IND) system has been developed [11]; this uses a four-step algorithm of datum definition, optimum distance calculation, viewpoint generation, and viewpoint clustering and selection. IND relies on initial object geometry, which can be obtained using a structure from motion or structured light projection technique. Other recent work [9] uses evolutionary algorithms to optimise coverage and viewpoint redundancy in a multi-sensor measurement network. Some approaches attempt to iteratively improve on a sparse initial network by adding more camera views in-situ; however, this approach requires a reasonable initial network and in-situ computation time which would hamper measurement speed. For example, Erat et al. [28] present a real-time online variant of view planning approach which accepts incoming views to the network if this view improves coverage of the scene based on a predefined coverage metric.

While there has been some work in this area, it is clear that automated view planning remains an open problem for multi-view optical CMSs. There is room for development of a general approach, based on a priori knowledge of an object and the nature of the CMS, which considers both viewpoint location and total number of viewpoints in the same optimisation process.

2. Methodology

2.1 Outline of the technique

For a given manufactured part, it is a complex task to directly identify how many images are necessary to fully cover the surface of the part, and the positions from which those images should be taken. A large number of images takes more time to acquire and is more computationally expensive to analyse. Furthermore, if the cameras are at unsuitable positions, accurate reconstruction of the object will not be possible. The optimisation of camera positions is greatly affected by the total number of camera positions required. Hence, for accurate and fast three-dimensional (3D) measurement by a multi-view optical CMS, it is necessary to first determine the number and positions of the images required to form an efficient network of camera viewpoints.

The proposed method for camera positioning is illustrated in Figure 1(a). Points on the surfaces of the computer aided design (CAD) data for a given artefact are sampled to approximately 10 000 points, we used the 'sample points' function in the open source software CloudCompare [29]. A technique for analysing which of these discretised surface points are visible from a given camera position has been developed; this technique is used in the optimisation procedure as follows. An initial local optimisation determines the single camera position which provides the highest surface coverage. Following this, the locally optimised position is used as a seed location for a global optimisation of n camera positions. The global optimisation uses a GA to maximise an objective function which considers the surface coverage, image overlap and inter-camera angles. Next, the process of global optimisation is repeated with increasing values of n until a threshold objective function value is achieved. These optimisation procedures are described in detail in Section 2.4. The method is validated using the experimental setup shown in Figure 1(c) on four example artefacts which are shown in Figure 2.

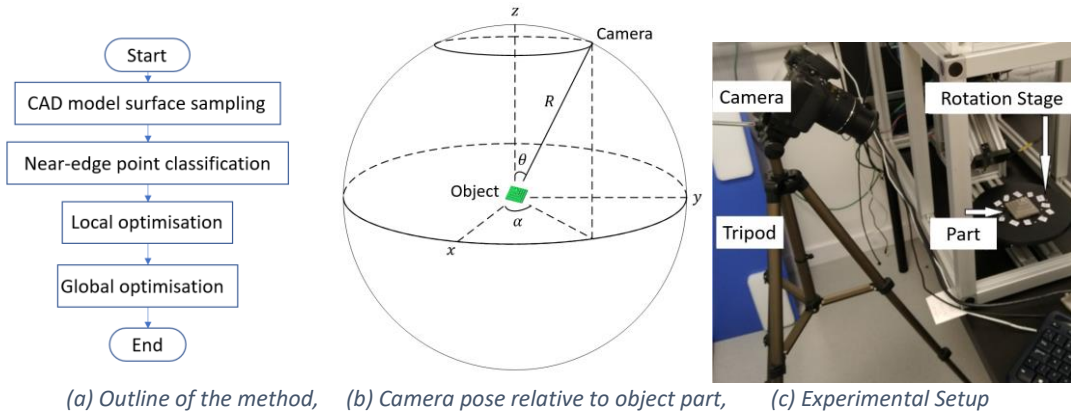


Figure 1 Outline of the method, camera pose parameterisation and experimental setup.

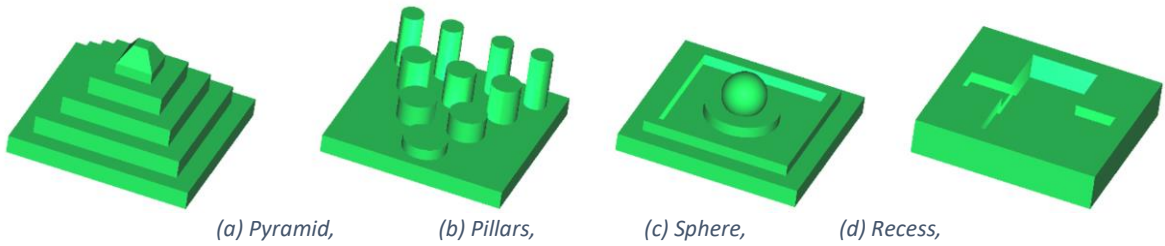


Figure 2 CAD data for four example artefacts (base sizes 50 mm × 50 mm).

To determine the potential camera poses, the working area is parameterised as shown in Figure 1(b). Two variable parameters are used to represent the camera pose in 3D: the azimuth angle ($0^\circ \leq \alpha < 360^\circ$) in the x, y plane, and the elevation angle ($0^\circ \leq \theta < 180^\circ$) with respect to the z axis. The principal axes of the cameras are set to be convergent at the object centre. A third parameter, the radius from the object centre R , must also be set. We fix R such that the cameras are all placed sufficiently far from the object centre such that increasing the value of R has a negligible impact on the number of visible points. We fix R at this point so that the angles produced by the optimisation do not depend on the field of view or resolution of the specific camera used (in this case a Nikon D3300). In the case of the example artefacts, the minimum radius at which the maximum number of surface points can be seen was found at $R = 500$ mm, therefore, R is fixed to this value for the rest of this paper.

2.2 Visible points analysis

There are several techniques to find which points on an object's surface are visible, given the camera's viewpoint relative to that object. These techniques can be classified as surface triangulation-based techniques, voxel-based techniques and point-based techniques [30]. We use a point-based analysis approach due to its high computational efficiency. However, the point-based technique has been shown to have poor performance at areas of high local curvature, such as sharp edges [31]. Therefore, we first classify the near-edge surface points; this allows us to use the more accurate but less efficient triangulation approach on the near-edge points, while using the more efficient point-based technique on the remaining surface points.

2.2.1 Triangulation-based technique

In the triangulation-based technique, the surfaces of the object are discretised into a set of tessellated triangles. The camera-to-object surface distance is computed by calculating the minimum distance from the camera centre O_c to the point P_i on the surface. For triangle vertices (V_0, V_1, V_2) , the ray-triangle intersection formulation is given by [32]

$$\begin{bmatrix} P_{ix} & V_{0x} - V_{1x} & V_{0x} - V_{2x} \\ P_{iy} & V_{0y} - V_{1y} & V_{0y} - V_{2y} \\ P_{iz} & V_{0z} - V_{1z} & V_{0z} - V_{2z} \end{bmatrix} \begin{bmatrix} D_i \\ u \\ v \end{bmatrix} = \begin{bmatrix} V_{0x} - O_{cx} \\ V_{0y} - O_{cy} \\ V_{0z} - O_{cz} \end{bmatrix}, \quad (2.1)$$

where D_i is the camera-to-object distance and (u, v) are the barycentric coordinates of the intersection point. If the point is visible, D_i should be the smallest distance that corresponds to a point in a given triangle. The triangulation intersection approach is effective but results in high computational costs, as the intersections need to be evaluated on all the points over all the triangles. The triangulation-based approach is, therefore, not efficient as the order of growth of the algorithm is $O(N_p \cdot N_\Delta)$, where N_p is the number of points and N_Δ is the number of triangles.

2.2.2 Point-based technique

A point-based technique, referred to as hidden point removal (HPR) [33, 34], is widely used in the areas of computer vision and graphics. HPR is composed of two steps: point inversion and convex hull computation. Point inversion reflects all points inside a bounding sphere to the outside of that sphere. The coordinate system which defines this inversion has its origin at the camera origin. The inversion can be defined mathematically as

$$\hat{p}_i = F(p_i) = p_i + 2(R_s - \|p_i\|) \frac{p_i}{\|p_i\|}, \quad (2.2)$$

where R_s is the sphere radius [32] and \hat{p}_i is the inverted coordinate corresponding to p_i . Points which are visible from a camera position, when transformed, now lie on the convex hull of the inverted point cloud. The convex hull calculation constructs a non-ambiguous representation of the convex hull of the inverted point cloud, thus allowing the visible points to be categorised. The order of growth of the convex hull calculation is $O(N_p \log(N_p))$ which is a much slower rate of growth than that of the triangulation approach and could be further improved through parallel computing.

Due to its higher efficiency when compared to the triangulation approach, the HPR technique is suitable for denser point clouds. However, disadvantages of the HPR technique are that it is sensitive to noise in the point cloud [34] and misclassification errors are expected to occur around regions of high local curvature [31]. In order to reduce the misclassification around the edges, an enhanced visible points analysis technique is proposed which combines the triangulation and HPR techniques and is described in the following section.

2.2.3 Enhanced visible point analysis technique

Since HPR misclassifies points around high-curvature areas, such as sharp edges, it is preferable that the points are first classified into two sets: the set of near-edge points P_e or the set of points remote from an edge P_o , which can be expressed by

$$\begin{aligned}
P_e &= \{p_i | D(p_i, e) < D_{th}\}, p_i \in P \\
P_o &= \{p_i | p_i \notin P_e\}, p_i \in P
\end{aligned}
\tag{2.3}$$

where P is the set of all surface points, D_{th} is a distance threshold and $D(p_i, e)$ is the minimum distance from the point p_i to an edge. In Standard Tessellation Language (STL) models, the CAD model is represented by a set of triangular faces. Edges can, therefore, be classified along triangular boundaries where the neighbouring triangular faces have large differences in the directions of their surface normals. Once the edges are located, all the surface points can be filtered by their Euclidean distance to the nearest edge and, therefore, categorised into either P_e or P_o according to equation (2.3). Points are then evaluated for visibility using either HPR if they are in P_e or by the triangulation-based intersection technique if they are in P_o . This enhanced visible point analysis pipeline is shown in Figure 3.

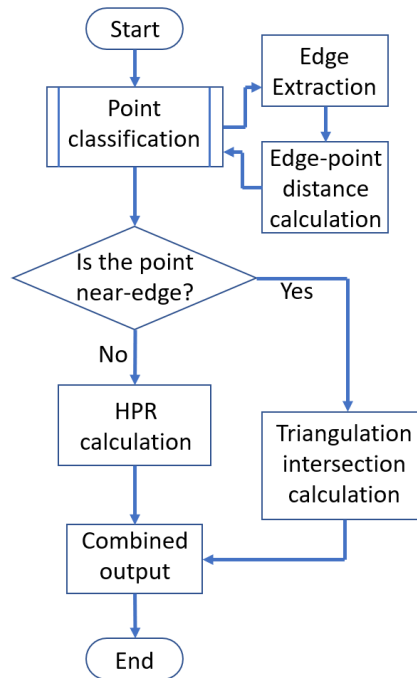


Figure 3 Enhanced visible points analysis technique .

As the distance threshold D_{th} increases, the proportion of points classified as near-edge increases. In order to decide at what value to set the distance threshold, D_{th} is varied from 0.01 mm to 5 mm. Figure 4 shows how changing D_{th} changes the resulting classification of surface points. It can be seen that there is some variation between the curves generated for the four objects. This variation between the four objects is due to the differing amounts and distributions of edges present in each object. However, the overall contours of the curves for each object is similar, with a clear change in gradient at 0.1 mm. As a result of this clear change in gradient, a distance threshold value of $D_{th} = 0.1$ mm is chosen. In the case of the four test artefacts, when using $D_{th} = 0.1$ mm, around 5% of the surface points are considered near-edge points, i.e. classified into the set P_e . In the case of a purely freeform object with no sharp edges, this approach would not be required. However, as the relative edge density of the part increases, selecting the threshold value through a convergence criteria on the gradient of the slope as shown in Figure 4 will provide a suitable value of D_{th} .

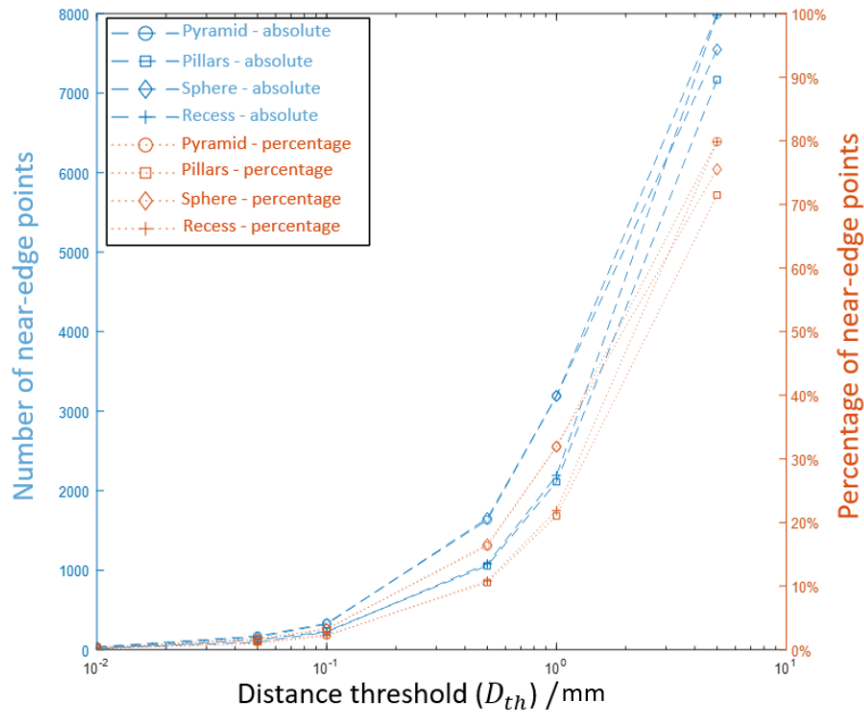


Figure 4 Near-edge point classification based on different threshold values for four objects.

Using this combined, enhanced technique of visible point analysis proffers an improved divide-and-conquer solution to determining the set of points which are visible. Compared to pure HPR analysis, the enhanced technique results in a reduction of misclassified points from 3% of the total points to 1% of the total points. Misclassification by pure HPR could be due to both visible points being incorrectly classified as not-visible, and not-visible points being misclassified as visible. Figure 5 shows the points which are misclassified when using pure HPR but are correctly classified when using enhanced visible point analysis as proposed.

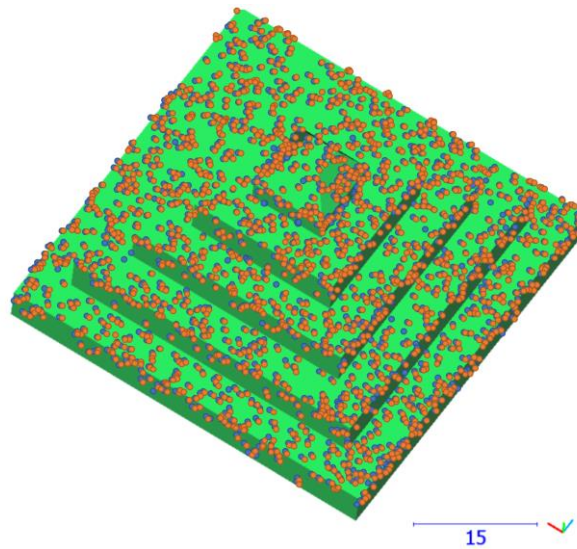


Figure 5 Misclassified points when using HPR which are correctly classified when using the proposed enhanced visible point analysis. Visible points classified as invisible are shown in blue, and invisible points classified as visible are shown in orange. Scale is in millimetres.

Table 1 compares the performance of the three possible approaches. It is clear that HPR is the most efficient and the triangulation-based method the least efficient. This makes sense as the order of growth of HPR with N_p number of surface points is $O(N_p \log(N_p))$ while for the triangulation based approach the order of growth is $O(N_p^2)$.

| Case | Triangulation-based | | HPR | | Enhanced HPR | | |
|------|---------------------|----------------|--------|----------------|--------------|----------------|-------------------------------------|
| | Time/s | Visible points | Time/s | Visible points | Time/s | Visible points | Reduction in misclassified points/% |
| 1 | 2.93 | 3151 | 0.09 | 3052 | 0.18 | 3054 | 2.02 |
| 2 | 2.93 | 4579 | 0.10 | 4605 | 0.20 | 4590 | 57.69 |
| 3 | 2.97 | 4593 | 0.10 | 4619 | 0.20 | 4614 | 19.23 |
| 4 | 3.09 | 4600 | 0.10 | 4642 | 0.19 | 4634 | 19.05 |
| 5 | 3.03 | 4645 | 0.10 | 4577 | 0.18 | 4574 | 4.41 |
| 6 | 3.19 | 4575 | 0.09 | 4615 | 0.22 | 4608 | 17.50 |
| 7 | 3.07 | 3751 | 0.06 | 3758 | 0.16 | 3757 | 14.29 |
| 8 | 2.95 | 3540 | 0.06 | 3548 | 0.17 | 3546 | 25.00 |
| 9 | 2.97 | 4687 | 0.09 | 4706 | 0.19 | 4696 | 52.63 |
| 10 | 3.01 | 4705 | 0.10 | 4716 | 0.20 | 4711 | 45.45 |

Table 1 Performance comparison of three visible point analysis methods: triangulation-based, HPR and enhanced HPR. Including reduction in misclassified points when using enhanced HPR.

It can be seen in Table 1 that our enhanced approach, while taking more time than pure HPR, is an order of magnitude faster than the triangulation approach. The enhanced HPR offers between 2% to 57% reduction in misclassified points over HPR; this creates a reasonable trade off between algorithmic efficiency and performance.

2.3 Optimisation scheme

Utilising the visible point analysis technique described above, we have developed an optimisation scheme for determining optimal camera positions. Former work in this area has assumed a fixed number of camera views [16] whereas in our proposed scheme the number of views can also be varied and optimised. Firstly, an initial camera position is found through a local optimisation process. Additional cameras are then added to a global optimisation process until an objective function threshold is achieved. The basic outline of this procedure is shown in Figure 6.

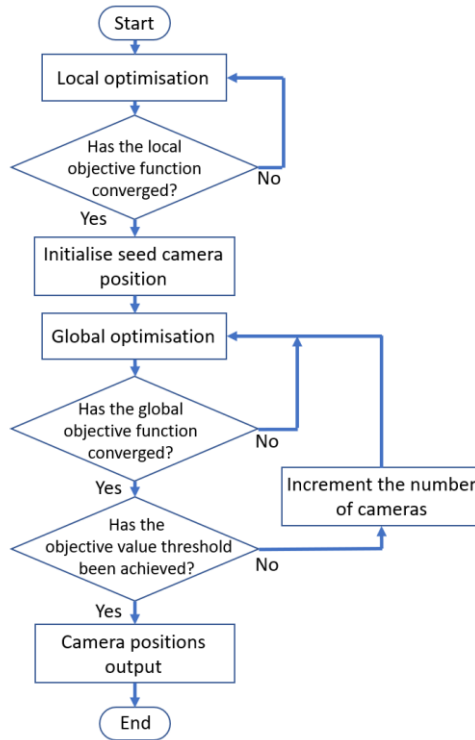


Figure 6 Optimisation scheme.

2.3.1 Local optimisation

In a first step, we determine the optimum position of a single camera based on surface coverage alone. The locally optimised position will then be used as a seed location from which to perform the global optimisation. To determine this camera location, we maximise the following objective function

$$F_{binary} = \sum_{k=1}^N [vis(p_k)], \quad (2.4)$$

where N is the total number of surface points, p_k is the k^{th} surface point and $vis(p_k)$ returns one if the point is visible and zero otherwise (using the previously described analysis). While a GA could be employed here, a simple search algorithm can be used as the search space for a single camera is well constrained.

The results of the local optimisation process for the four example artefacts are shown in Figure 7. The pillars artefact has two equally optimal camera positions due to its two-fold rotational symmetry, while the remaining artefacts have four equally optimal positions due to their four-fold symmetry. In the case where multiple positions are equally optimal, one of these positions can be chosen arbitrarily.

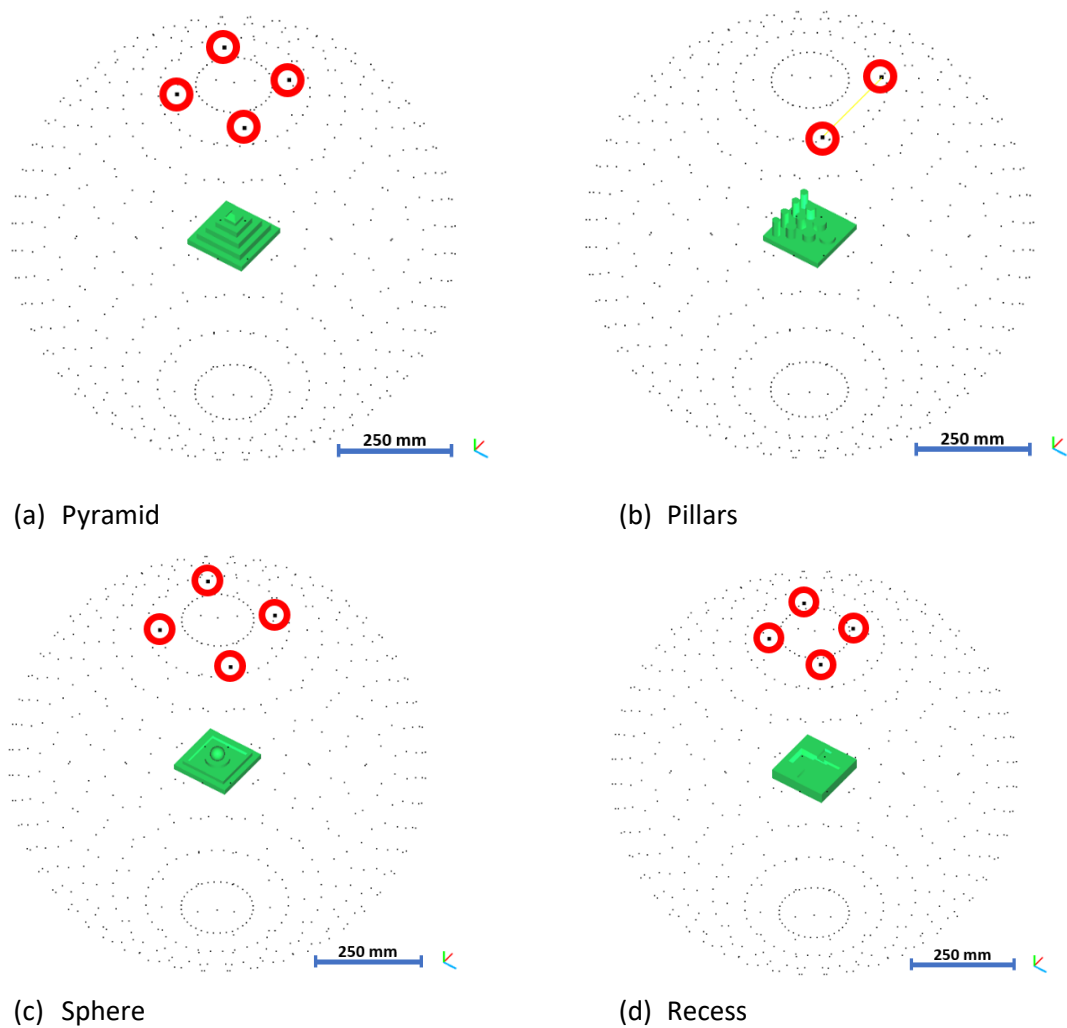


Figure 7 Optimal camera locations for the four example artefacts.

As can be seen, excluding the pillars artefact, the optimum camera positions in each case are aligned with the four corners of that artefact. Furthermore, it can be inferred that the optimum camera elevation angle depends to the relative height of the object, at 12° for the shallow recess artefact and 18° for the more prominent pyramid object.

2.3.2 Global optimisation

After the seed camera location is found through local optimisation, a global optimisation procedure is conducted from this location. The global optimisation process aims to optimise for two criteria: that each surface point is seen by a minimum of four cameras and an inter-camera convergence angle of 90° for all cameras, at all surface points. Attempting to view each surface point from four camera locations maximises surface coverage while promoting overlap between images. Additionally, promoting a camera convergence angle of 90° has been shown in previous work to provide the highest reconstruction accuracies [8, 29].

In contrast to the local optimisation procedure, we now consider multiple camera images at once. The global objective function is given by

$$F_{global} = \frac{1}{4 \cdot N} \cdot \left(\omega \cdot \sum_{i=1}^n \sum_{k=1}^N [\cos(\gamma_{ik})] + \frac{(\omega-1)}{2 \cdot (n-1)} \cdot \sum_{i=1}^n \sum_{j=i+1}^n \sum_{k=1}^N [\sin(\beta_{ijk})] \right) \quad (2.6)$$

where ω is a weighting coefficient, n is the total number of camera images, γ_{ik} is the angle at the intersection between a ray cast from camera c_i and the surface normal at surface point p_k , and β_{ijk} is the triangulation angle between the ray-lines projected from camera c_i and camera c_j , which intersect at surface point p_k . In the case where there are more than four cameras in the optimisation, the value of $\sum_{k=1}^N [\cos(\gamma_{ik})]$ may exceed four – it is, however, capped at this value. Capping this value ensures that it is more optimal for every point to be seen by a few cameras, than for a single point to be seen by many cameras. Capping this value at four implies the optimal score is given when every surface point is viewed from at least four camera positions. The first half of the objective function (which considers γ_{ik}) is similar to F_{binary} but has been adapted to loop over all surface points for all camera positions. It also now considers not just if a point is visible but the cosine of γ_{ik} for all visible surface points from a given view. This gives a higher weighting to views which are orthogonal to surface faces which is desirable for high quality reconstructions. The global optimisation procedure is conducted as follows. The objective function is maximised for four cameras by a GA, these four cameras are initialised using the seed position found in the local optimisation procedure. When this optimisation is complete, if the objective function has not reached a 95% threshold value, then an additional two cameras are inserted and the optimisation is reapplied. A convergence threshold of 95% was selected as it provides similar reconstruction results to a higher threshold value at a much smaller computational cost. As n in the optimisation increases, the number of inter-camera angles β_{ijk} scales with $\frac{1}{2}(n^2 - n)$. To prevent the inter-camera component dominating F_{global} , the value of the weighting coefficient is, therefore, set by

$$\frac{\omega}{1-\omega} = \frac{n-1}{2} \quad (2.7)$$

In our implementation, the default MATLAB GA [35] was used with the following modifications: a population size of 500, a cross-over rate of 80% and a 5% elite population classification rate. In order to ease the computational load, the algorithm uses flexible parameters that allow for a small population with broad tolerances at low numbers of camera positions and larger populations with narrower tolerances at high numbers of camera positions. Figure 9 shows the optimisation results for the four artefacts.

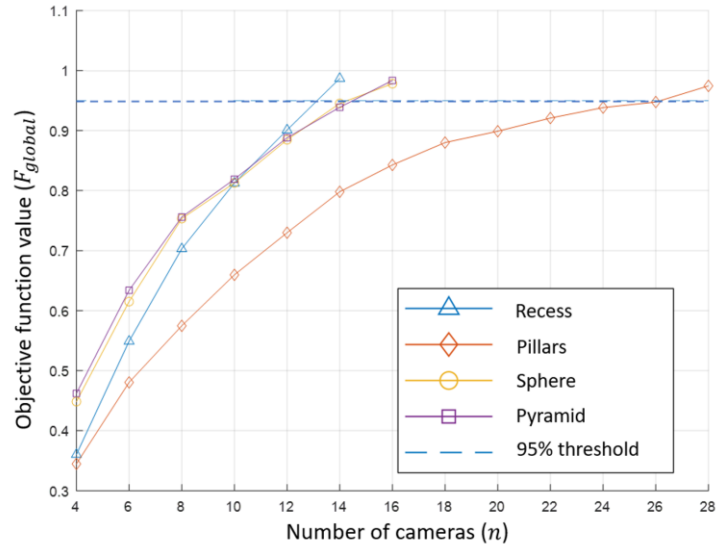


Figure 9 Objective function optimisation for the four test artefacts.

Convergence to the threshold criteria is achieved with a different number of cameras for each object, the pyramid and sphere require fourteen images, the recess only twelve images and the pillars require twenty-two images. The differing minimum number of camera viewpoints required corresponds to the relative complexity of each artefact and the number of occlusions due to that artefact's features. The time to run the GA varies with the number of cameras in the simulation, the computer hardware, and the specific implementation details of the algorithm. In this case using a Lenovo PC (Lenovo PC Think Center M910s i3-7100 3.9 GHz, 8G RAM, 1T HDD) for twelve camera positions, the GA took around two hours for optimisation, while for twenty camera positions, the GA took around seven hours for optimisation. These times are likely to be significantly reduced through a parallel implementation and faster hardware.

3. Results

Using the photogrammetry setup shown in Figure 1 (c), images at optimised positions were captured from a Nikon D3300 DSLR camera using a 40 mm focal length and ISO 400. These images were then used to reconstruct point clouds of the artefacts using the photogrammetry software Agisoft© Metashape [36]. The point clouds were registered to their ground truth models using the iterative closest point (ICP) algorithm in CloudCompare **Error! Reference source not found.** Lastly, the deviations of the points from the ground truth models were analysed to assess the quality of the reconstructions.

To acquire ground truth models of the artefacts, a stereo fringe projection system (GOM ATOS [37]) was used as an industrial comparison and a contact CMM was employed to create reference measurements. These measured ground truth models of the manufactured artefacts, rather than CAD models, are used for comparison because the manufacturing process of the artefacts can contribute significant shape changes relative to the intended design model. As such, when comparing against a CAD model it would be impossible to tell if a deviation was due to measurement error or manufacturing error. The experiment is conducted with an ATOS GOM Core 300 from eight different positions with field of view 300 mm × 200 mm, probing size error 0.006 mm, and sphere spacing error 0.020 mm (as quoted by the manufacturer). In section 3.3, the reference measurement is obtained using a Mitutoyo Crysta Apex S7106 contact CMM system with a SP25 probe attached. The contact probe has maximum

permissible probing and scanning errors of $1.7\ \mu\text{m}$ and $2.2\ \mu\text{m}$ respectively as specified by the instrument manufacturer.

3.1 Photogrammetry using optimised camera positions

The optimisation process proposed in section 2.4 was implemented. Two measurements were taken of each artefact, one set with twelve optimised camera images and one set with eighteen images. Images captured at the optimised positions were used to reconstruct textured dense point clouds of the artefacts through the photogrammetric pipeline of Metashape. First, given a set of images, Metashape computes the intrinsic camera properties and re-evaluates the relative positions of the camera viewpoints. Sparse 3D points are then triangulated and refined after feature points are detected and matched between images. Finally, a densification process expands the sparse point clouds from thousands of points to millions of points. Figure 10 (a) shows the dense and textured point cloud of the pyramid artefact using twelve images. A qualitative improvement in the point cloud can be observed when the number of images was increased to eighteen, as shown in Figure 10 (b). These reconstruction results align well with the high value of the objective function for the artefacts when using eighteen camera positions, as shown in Figure 9.

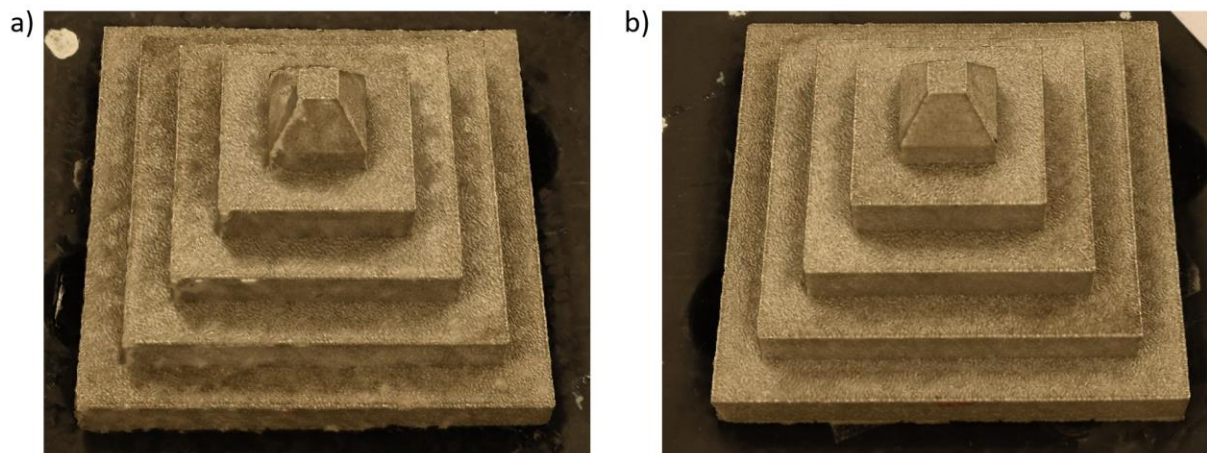


Figure 10 Reconstruction results using proposed twelve (a) and eighteen (b) optimised camera positions for the pyramid artefact.

Further to the qualitative analysis, the difference in reconstruction accuracies for the twelve and eighteen image reconstructions are given in Figure 11. Reconstructed points using twelve and eighteen optimised images were compared with the reference triangular-mesh model obtained from the commercial GOM ATOS instrument.

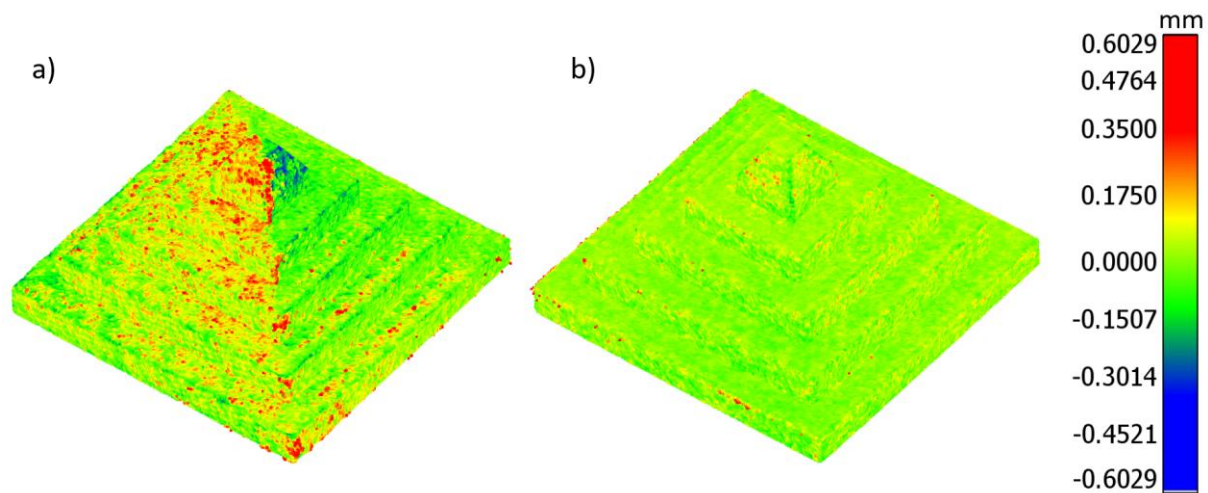


Figure 11 Deviations in measurement results from the reference GOM ATOS mesh when using images from (a) twelve and (b) eighteen camera positions.

In Figure 11, the point clouds for the pyramid artefact were compared with the model produced by the GOM ATOS system. To remove possible outliers, only point-to-mesh (PTM) distances within four standard deviations of the mean are shown. For the reconstruction using twelve images, shown in Figure 11 (a), significant discrepancies are observed over the corners, some upper surfaces and the vertical walls of the pyramid. However, when using eighteen optimised images, as shown in Figure 11 (b), the discrepancies are much diminished around the corners and are barely observed on most flat surfaces of the object. In addition, the root-mean-square (RMS) value of the PTM distances is 0.101 mm for twelve camera positions compared to 0.052 mm for eighteen camera positions. The loss in quality when using twelve optimised images rather than eighteen images as suggested by the optimisation demonstrates that using a fewer number of camera positions than suggested by the GA does, in fact, lead to a decrease in photogrammetric reconstruction quality.

3.2 Comparison of equally spaced and optimised camera positions

To assess the effectiveness of the proposed camera positioning technique, reconstructions using the optimised camera positions were compared with reconstructions using an equal number of camera images, positioned evenly around the artefact. The use of camera positions equally spaced on a circle surrounding an object is a common practice in small-scale photogrammetry [38-41]. To enable this comparison, throughout sections 3.2 and 3.3 the elevation angle is fixed at 35° and only the azimuth angles are varied.

Reference measurements obtained by the GOM ATOS fringe projection system are used to evaluate the deviation of the point clouds for the pyramid and pillar artefacts. The standard deviations of the PTM distances of the reconstructions are shown in Figure 12 over a range of ten to thirty total camera positions. The evaluation of the deviations is repeated on five sets of measurement data, the variations in the standard deviation of the repeated measurements are shown by error bars. Generally, the standard deviations of the pillar artefact are higher than the pyramid artefact, likely because of the greater self-occlusion caused by pillars. When the number of camera positions is less than twenty, the proposed technique performs with clearly lower deviation than the equally distributed camera positions. Additionally, the error bars are, on average, wider for the equally spaced camera positions, indicating improved stability with the proposed technique. When the number of camera positions is more than twenty-two, the two techniques perform comparably. The similarity in performance above

twenty-two camera locations is because a high number of camera positions allows most regions on the artefact's surface to be sufficiently covered without optimisation.

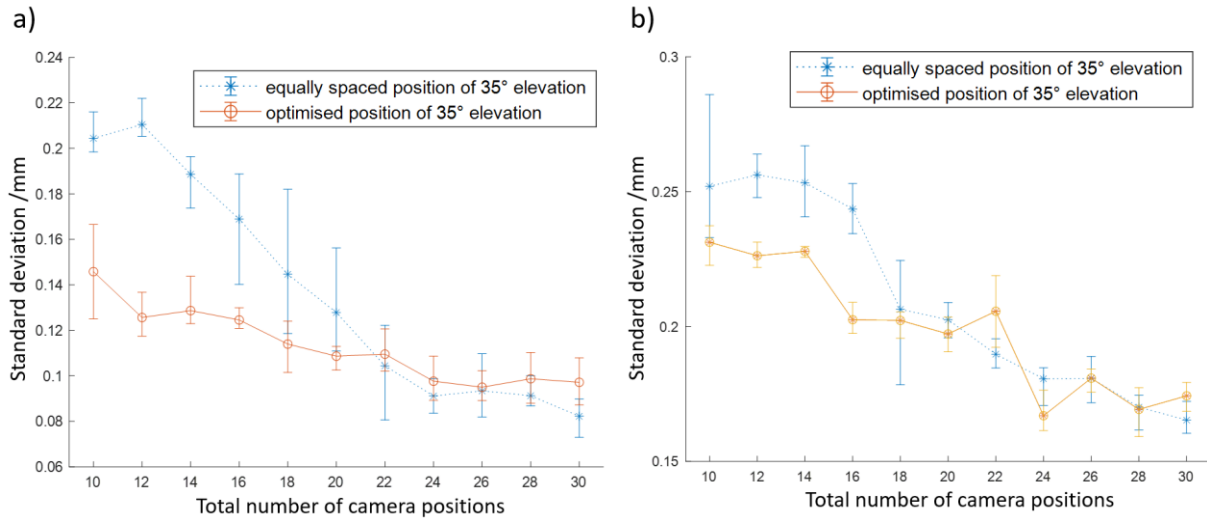


Figure 12 Comparison of the standard deviation in PTM distances for the pyramid artefact (a) and the pillars artefact (b) for both optimised and equally spaced camera imaging positions.

As can be seen in Figure 12(b), the reconstruction with sixteen optimised image positions performs similarly to a reconstruction using twenty-two un-optimised image positions. Table 2 shows a comparison in the performance of the reconstruction algorithm for the reconstructions shown in Figure 12(b).

| Number of images | Optimised camera locations | | | Equally spaced camera locations | | |
|------------------|-------------------------------|--------------------------------|----------------------------|---------------------------------|--------------------------------|----------------------------|
| | Time to generate depth maps/s | Time to generate point cloud/s | Number of points generated | Time to generate depth maps/s | Time to generate point cloud/s | Number of points generated |
| 10 | 11 | 26 | 1 376 044 | 11 | 20 | 1 186 167 |
| 12 | 15 | 33 | 1 385 261 | 32 | 28 | 1 374 713 |
| 14 | 26 | 44 | 1 357 144 | 73 | 38 | 1 376 383 |
| 16 | 27 | 62 | 1 412 859 | 51 | 48 | 1 305 737 |
| 18 | 22 | 83 | 1 423 958 | 57 | 66 | 1 275 405 |
| 20 | 29 | 106 | 1 357 347 | 44 | 84 | 1 249 084 |
| 22 | 36 | 146 | 1 358 505 | 46 | 99 | 1 210 973 |
| 24 | 39 | 167 | 1 368 261 | 53 | 209 | 1 435 513 |
| 26 | 53 | 224 | 1 347 636 | 63 | 108 | 1 207 208 |
| 28 | 56 | 283 | 1 346 136 | 67 | 192 | 1 153 688 |

| | | | | | | |
|----|----|-----|-----------|----|-----|-----------|
| 30 | 95 | 439 | 1 498 454 | 65 | 265 | 1 450 326 |
|----|----|-----|-----------|----|-----|-----------|

Table 2 Comparison of reconstruction performance for equally spaced and optimised camera locations. Shown in bold are the values for sixteen optimised image positions and twenty-two un-optimised image positions which were shown to perform similarly in Figure 12(b).

As can be seen, reconstruction using sixteen optimised image positions takes much less time to generate both depth maps and the dense point cloud, while producing 200 000 more points, than using twenty-two un-optimised image positions. Our method takes consistently less time to produce depth maps than the un-optimised approach and produces point clouds with consistently many more points.

To visually compare the analysis of the measured point clouds, the deviations of point clouds of the pyramid and pillar artefacts obtained from the two sets of camera positions are juxtaposed in Figure 13. Two sets of fourteen camera positions, one equally spaced and the other optimised, are used for reconstruction in this case.

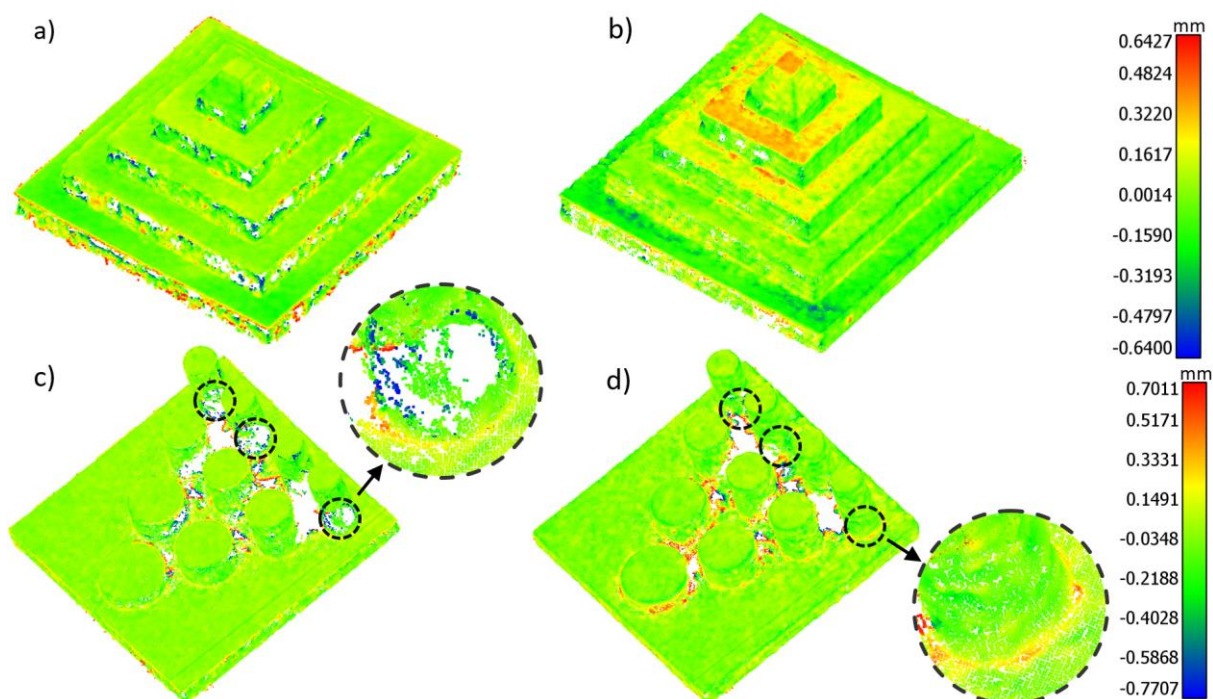


Figure 13 Comparison of the PTM deviations of the pyramid and pillar point clouds from GOM results. (a) and (b) show the equally spaced and optimised results respectively for the pyramid artefact, (c) and (d) show the same for the pillars artefact.

It can be seen from Figure 13 that the deviations are lower in the optimised cases, especially in the vertical faces. Furthermore, the coverage of the surfaces is far more complete when using the optimised positions; this is seen optimised on the vertical walls of the pyramid and in the inset images at the base of the pillars. Ultimately, using the optimised camera positions results in more accurate, complete and stable reconstruction when compared to using the same number of equally spaced images; and furthermore, requires fewer total images to achieve accurate reconstruction.

3.3 Comparison with CMM data

The 3D point clouds of the pyramid artefact are further compared with measurements carried out using a CMM. Comparison to a CMM measurement is carried out for reconstructions resulting from both the optimised and the equally spaced camera positions. In Figure 14, a point cloud generated by the CMM is compared with meshes obtained from Metashape photogrammetric reconstruction using eighteen camera positions. A probe tip diameter of 1 mm was used in scanning mode to measure contours on the surface of the pyramid artefact. Points were sampled at 10 μm along each contour and the spacing between the contours was 200 μm . The gaps seen in the two measurements are due to regions that were omitted by the CMM path program to avoid potential collision of the part with the stem of the stylus.

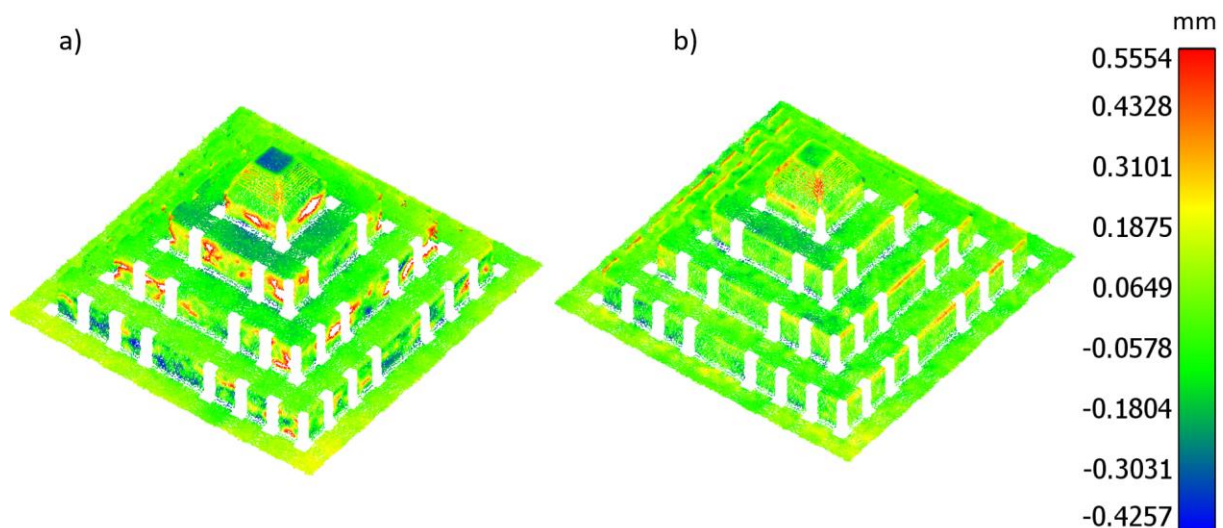


Figure 14 CMM comparison of the reconstructions resulting from equally spaced camera positions (a) and optimised positions (b).

The distributions of the PTM distances are observed to be consistent with the PTM distances from the GOM ATOS system. Points omitted on the vertical walls of the pyramid in Figure 14 (a) have distances that exceed the range on the colour scale. In addition, the RMS PTM distances reduce from 0.145 mm to 0.095 mm when using the optimised camera positions rather than the equally spaced positions.

In general, using both contact and non-contact reference measurement techniques, the point clouds reconstructed from images captured at the optimised camera positions are shown to be more accurate and complete. This work shows that using an initial CAD model of an object, the combinations of camera positions can be optimised to improve optical 3D coordinate measurements.

Conclusions

A technique for the optimisation of camera positions for optical coordinate measurement is presented in this paper. Camera positions used in optical coordinate measurements are determined based on visible point analysis and global optimisation. From an object's computer aided design model, the surfaces are discretised into points. An enhanced visible point analysis technique is used to determine which of these surface points are visible from a given camera position. The enhanced visible

point analysis technique adopts a combination of the use of a hidden point removal algorithm for the majority of the surface points, and a triangulation-based intersection algorithm for the near-edge points. The enhanced approach is used to decrease the misclassification of visible points. The optimisation technique determines not only the optimal camera positions for a given number of total camera positions, but also the minimum number of total camera positions required to meet a threshold criterion. Iterating the optimisation for increasing numbers of camera positions allows the minimum required number of camera positions to be determined for a given object, allowing more efficient computation during reconstruction.

A proposed objective function which considers the visible points, as well as image overlap and inter-camera angles, is presented. A genetic algorithm is employed for global optimisation of the camera positions with respect to this objective function.

Comparisons of results acquired using the proposed technique with results from equally spaced camera positions are conducted. The quality of these reconstructions is analysed by comparison with an industrial optical fringe projection instrument and a tactile coordinate measurement machine. It is shown that using the optimised positions improves the coverage of an object's surface and produces point clouds with lower point-to-mesh distances when compared to the reference measurements. Furthermore, it is demonstrated that a measurement using a lower number of optimised camera positions performs as well as, or in some cases better than, a measurement using a higher number of un-optimised camera positions. By enabling the use of fewer images while maintaining reconstruction quality, measurement time and data processing time can both be reduced using the optimised camera positions. Although the proposed technique is shown to be beneficial, there are still some issues that require further investigation; among them, improving the time for conducting the optimisation and investigating the effects of non-uniform lighting on visibility. These suggested improvements will form the basis for future work that we are conducting to develop an automated optical coordinate measurement pipeline [42,43].

Acknowledgements

This work was funded by the China Scholarship Council No.201808320185 and EPSRC (grants EP/M008983/1 and EP/L016567/1) and was carried out in the University of Nottingham. Our sincere thanks go to Sofia Catalucci, Amrozia Shaheen and others in the Manufacturing Metrology Team at the University of Nottingham.

References

- [1] Liu T, Burner A W, Jones T W, Barrows D A 2012 Photogrammetric techniques for aerospace applications *Prog. Aerosp. Sci.* **54** 1–58
- [2] Schuch H, Nogueira C L, Rutz F R, Rens K L 2019 Photogrammetric modelling of a stone bridge for structural analysis *Proc. ARCH2019* 273-279
- [3] Baqersad J, Poozesh P, Niezrecki C, Avitabile P 2017 Photogrammetry and optical methods in structural dynamics—A review *Mech. Syst. Signal Pr.* **86** 17-34
- [4] Leach R K, Bourell D, Carmignato S, Donmez A, Senin N, Dewulf W 2019 Geometrical metrology for metal additive manufacturing *CIRP Annals* **68** 677-700
- [5] Płowucha W, Jakubiec W, Wojtyła M 2016 Possibilities of CMM software to support proper geometrical product verification *Proc. 14th CIRP CAT-2016* **43** 303-8

- [6] Zha X 2017 *Research on Process Planning and Program Generation Technology for Key Parts of Marine Diesel Engine* (Master Thesis, Jiangsu University of Science and Technology)
- [7] Mason S, Grun A 1995 Automatic sensor placement for accurate dimensional inspection *Comput. Vis. Image Und.* **16** 454-67
- [8] Tarabanis K, Allen P, Tsai R 1995 A survey of sensor planning in computer vision *IEEE Trans. Robot. Autom.* **11** 86-104
- [9] Rangel E, Costa D, Loula A 2019 On redundant coverage maximization in wireless visual sensor networks: Evolutionary algorithms for multi-objective optimisation *Appl. Soft Comput.* **82** 105578
- [10] Barazzetti L 2017 Network design in close-range photogrammetry with short baseline images *ISPRS Ann. Photogramm. Remote Sens. Spatial Inf. Sci.* 17-23
- [11] Ahmadabadian A, Robson S, Boehm J, Shortis M 2014 Stereo-imaging network design for precise and dense 3D reconstruction *The Photogram. Rec.* **29** 317-36
- [12] Mavrincac A, Chen X 2013 Modeling coverage in camera networks: a survey *Int. J. Comput. Vis.* **101** 205-26
- [13] Singh R, Panchal V, Singh B 2018 A review on genetic algorithm and its applications *Proc. 2nd ICXGCloT* 376-380
- [14] Kudjo P, Ocquaye E, Ametepe W 2017 Review of genetic algorithm and application in software testing *Int. J. Comput. Appl.* **160** 1-6
- [15] Whitley D 1994 A genetic algorithm tutorial *Stat. Comput.* **4** 65-85
- [16] Bhoskar M, Kulkarni M, Kulkarni M, Patekar M, Kakandikar G, Nandedkar V 2015. Genetic algorithm and its applications to mechanical engineering: A review *Materials Today: Proceedings* **2** 2624-30
- [17] Mahalakshmi M, Kalaivani P, Nesamalar E K 2013 A review on genetic algorithm and its applications *Int. J. Comput. Algorithm* **2** 415-23
- [18] Olague G, Mohr R 2002 Optimal camera placement for accurate reconstruction *Pattern Recognit.* **35** 927-44
- [19] Sun J, He H, Zeng D 2016 Global calibration of multiple cameras based on sphere targets *J. Sens* **16** 77
- [20] Liu Z, Meng Z, Gao N, Zhang Z 2019 Calibration of the relative orientation between multiple depth cameras based on a three-dimensional target *J. Sens* **19** 3008.
- [21] Feng H, Wu G, Feng M, Cen M, Liu Y 2018 Research on global measurement method based on multi-cameras *Proc. IOP Conf. SER* **382** 52039
- [22] Feng M, Jia X, Wang J, Feng S, Zheng T 2017 Global calibration of multi-cameras based on refractive projection and ray tracing *J. Sens* **17** 2494
- [23] Xing Z, Yu J, Ma Y 2017 A new calibration technique for multi-camera systems of limited overlapping field-of-views *Proc. IEEE IROS* 5892-5899
- [24] Gai S, Da F, Tang M 2019 A flexible multi-view calibration and 3D measurement method based on digital fringe projection *Meas. Sci. Technol.* **30** 25203
- [25] Ren F, Wang Z, Qian J, Liang Y, Dang S, Cai Y, Bianco P R, Yao B, Lei M 2019 Multi-view object topography measurement with optical sectioning structured illumination microscopy *Appl. Opt.* **58** 6288-6294
- [26] Olague G 2001 Autonomous photogrammetric network design using genetic algorithms *Applications of Evolutionary Computing, Springer Berlin Heidelberg* 253-363
- [27] Carrivick J L, Smith M W, Quincey D J 2016 *Structure from Motion in the Geosciences* John Wiley & Sons
- [28] Erat O, Hoell M, Haubenwallner K, Pirchheim C, Schmalstieg D 2019 Real-time view planning for unstructured lumigraph modeling *IEEE T. Vis. Comput. Gr.* **25** 3063-72
- [29] <http://www.cloudcompare.org/>

- [30] Alsadik B, Gerke M, Vosselman G 2014 Visibility analysis of point cloud in close range photogrammetry *ISPRS Ann. Photogramm. Remote Sens. Spatial Inf. Sci.* **172** 9-16
- [31] Mehra R, Tripathi P, Sheffer A, Mitra N 2010 Visibility of noisy point cloud data *Comput. Graph.* **34** 219-30
- [32] Moller T, Trumbore B 1997 Fast, minimum storage ray-triangle intersection *J. Graph. Tools* 21-8
- [33] Katz S, Tal A, Basri R 2007 Direct visibility of point sets *ACM TOG* **26** 24
- [34] Katz S, Tal A 2015 On the visibility of point clouds *The IEEE ICCV* 1350-8
- [35] <https://www.mathworks.com>
- [36] <https://www.agisoft.com/>
- [37] <https://www.gom.com/>
- [38] Lavecchia F, Guerra M G, Galantucci L M 2018 Performance verification of a photogrammetric scanning system for micro-parts using a three-dimensional artifact: adjustment and calibration. *Int. J. Adv. Manuf. Tech.* **96** 4267-79
- [39] Muralikrishnan B, Phillips S, Sawyer D 2016 Laser trackers for large-scale dimensional metrology: A review *Prec. Eng.* **44** 13-28
- [40] Percoco G, Guerra MG, Sanchez Salmeron A J, Galantucci L M 2017 Experimental investigation on camera calibration for 3D photogrammetric scanning of micro-features for micrometric resolution *Int. J. Adv. Manuf. Tech.* **91** 2935-47
- [41] Sims-Waterhouse D, Piano S, Leach R K Verification of micro-scale photogrammetry for smooth three-dimensional object measurement *Meas. Sci. Technol.* **28** 55010
- [42] Eastwood J, Sims-Waterhouse D, Piano S, Weir R, Leach R K 2019 Autonomous close-range photogrammetry using machine learning *Proc. 14th ISMTII*, Niigata, Japan
- [43] Eastwood J, Zhang H, Isa M, Sims-Waterhouse D, Leach R K, Piano S 2020 Smart photogrammetry for three-dimensional shape measurement *Proc. SPIE* **11352** 113520A